GEOPHYSICS, VOL. 53, NO. 11 (NOVEMBER 1988); P. 1425–1436, 16 FIGS., 1 TABLE.

Fourth-order finite-difference *P-SV* seismograms

Alan R. Levander*

ABSTRACT

I describe the properties of a fourth-order accurate space, second-order accurate time, two-dimensional *P-SV* finite-difference scheme based on the Madariaga-Virieux staggered-grid formulation. The numerical scheme is developed from the first-order system of hyperbolic elastic equations of motion and constitutive laws expressed in particle velocities and stresses. The Madariaga-Virieux staggered-grid scheme has the desirable quality that it can correctly model any variation in material properties, including both large and small Poisson's ratio materials, with minimal numerical dispersion and numerical anisotropy. Dispersion analysis indicates that the shortest wavelengths in the model need to be sampled at 5 gridpoints/wavelength. The scheme can be used to accurately simulate wave propagation in mixed acoustic-elastic media, making it ideal for modeling marine problems. Explicitly calculating both velocities and stresses makes it relatively simple to initiate a source at the free-surface or within a layer and to satisfy free-surface boundary conditions. Benchmark comparisons of finite-difference and analytical solutions to Lamb's problem are almost identical, as are comparisons of finite-difference and reflectivity solutions for elastic-elastic and acoustic-elastic layered models.

INTRODUCTION

Explicit finite-difference methods have assumed a prominent role in forward modeling in computational seismology because of their ability to accurately model wave propagation in laterally heterogeneous media. Unfortunately, explicit schemes are computationally expensive, requiring large amounts of computer memory to model exploration-scale problems. Currently only two-dimensional (2-D) and small three-dimensional (3-D) problems are feasible. A means of reducing computation time and memory requirements in finite-difference schemes is to use higher order finite-difference approximations to spatial and temporal derivatives (Dablain, 1986). While higher order finite-difference spatial operators can reduce computation costs for *P-SV* modeling, the development of higher order spatial operators which are stable and accurate for high Poisson's ratio materials and for mixed acoustic and elastic media has proven to be difficult (see Bayliss et al., 1986, for one example).

Madariaga (1976) developed a staggered-grid, finite-difference scheme based on the first-order coupled elastic equations of motion and constitutive laws expressed in particle velocities and stresses, which he used to model an expanding circular crack in an elastic space. Virieux (1984, 1986) adapted this scheme to general forward modeling of *SH* and *P-SV* waves in a 2-D Cartesian system. Both Madariaga's finite-difference operators and those of Virieux were second-order accurate in the time increment Δt and the space increment h. These are referred to as $O(\Delta t^2, h^2)$ schemes. To minimize grid dispersion and grid anisotropy, the spatial sampling required is at least 10 gridpoints/wavelength. The $O(\Delta t^2, h^2)$ *P-SV* staggered-grid scheme has several desirable qualities which are important for seismic exploration modeling. In particular, (1) the staggered-grid scheme is stable for all values of Poisson's ratio, making it ideal for modeling marine exploration problems or problems with high Poisson's ratio materials; (2) grid dispersion and grid anisotropy are small and relatively insensitive to Poisson's ratio; (3) surface or buried sources can easily be initiated; and (4) free-surface boundary conditions are easily satisfied. Some or all of these features are usually lacking from finite-difference schemes developed from the second-order coupled elastic equations expressed in displacements (e.g., Kelly et al., 1976).

In this paper I describe a second-order accurate time, fourth-order accurate space, $O(\Delta t^2, h^4)$, formulation of the 2-D Madariaga-Virieux staggered-grid scheme, investigate its dispersion properties, and describe benchmark tests of the finite-difference scheme. The use of fourth-order or higher-order accurate finite-difference approximations to spatial derivatives is an established means of reducing the spatial sampling required to accurately simulate wave propagation in finite-difference schemes (Alford et al., 1974; Dablain, 1986). In 2-D finite-difference modeling, the mesh size necessary to solve a

Manuscript received by the Editor January 25, 1988; revised manuscript received May 4, 1988.
*Department of Geology and Geophysics, Rice University, P.O. Box 1892, Houston, TX 77251-1892.

given model is proportional to the square of the maximum frequency desired in the solution. For constant bandwidth, a linear reduction in spatial sampling resulting from use of a higher order operator provides a geometric savings in computer memory (Dablain, 1986). The computational savings are somewhat less than geometrical because the reduction in nodes and the larger time step are balanced against the increased operator length.

FORMULATION

In a 2-D Cartesian system with the x axis horizontal and positive to the right, and the z axis positive down (Figure 1), the *P-SV* equations of motion are

$$\rho \frac{\partial u_t}{\partial t} = \frac{\partial \tau_{xx}}{\partial x} + \frac{\partial \tau_{xz}}{\partial z}$$

and (1)

$$\rho \frac{\partial w_t}{\partial t} = \frac{\partial \tau_{zx}}{\partial x} + \frac{\partial \tau_{zz}}{\partial z};$$

and the constitutive laws for an isotropic medium are

$$\tau_{xx} = (\lambda + 2\mu) \frac{\partial u}{\partial x} + \lambda \frac{\partial w}{\partial z},$$

$$\tau_{zx} = \mu\left(\frac{\partial u}{\partial z} + \frac{\partial w}{\partial x}\right), \quad (2)$$

and

$$\tau_{zz} = (\lambda + 2\mu) \frac{\partial w}{\partial z} + \lambda \frac{\partial u}{\partial x},$$

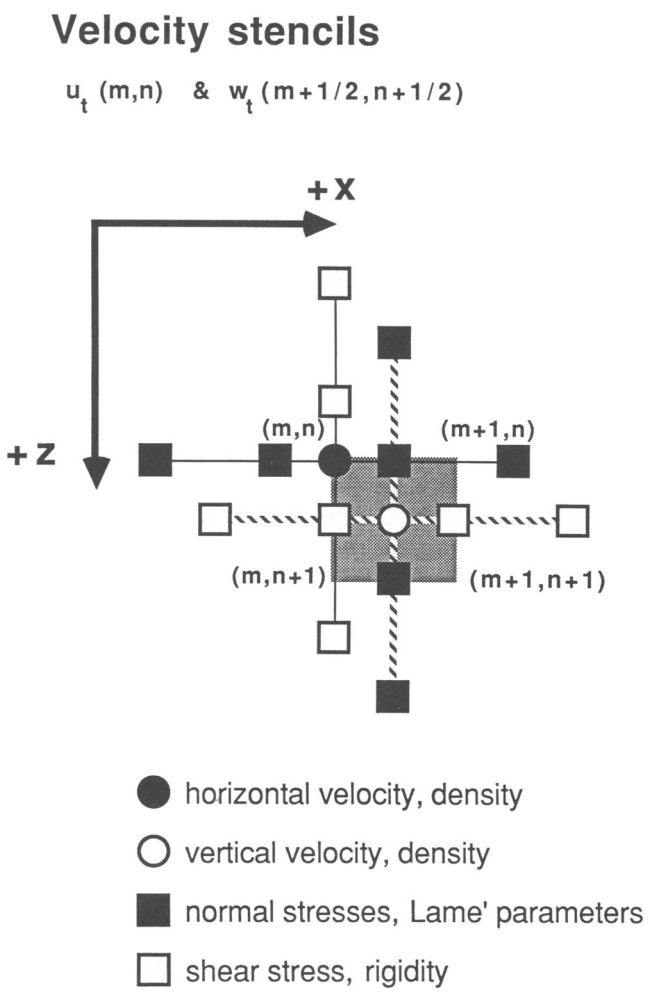

FIG. 1. Staggered finite-difference grid and spatial stencils for the velocity update. The gray square has area h^2. The corners of the square are at the grid points (m, n), $(m + 1, n)$, $(m + 1, n + 1)$, and $(m, n + 1)$. For the stencils of the single node in Figures 1 and 2, the horizontal velocity is defined at (m, n), vertical velocity at the half indices $(m + 1/2, n + 1/2)$, normal stresses at $(m + 1/2, n)$, and shear stress at $(m, n + 1/2)$. Velocity components are defined on the time levels $\ell - 1/2$ and $\ell + 1/2$, whereas stress components are defined on the levels ℓ and $\ell + 1$. The spatial stencil for horizontal velocity is shown as a thin solid line with the stress nodes used in the update. The spatial stencil for the vertical velocity is shown as a thin hachured line with the stress nodes used in the update.

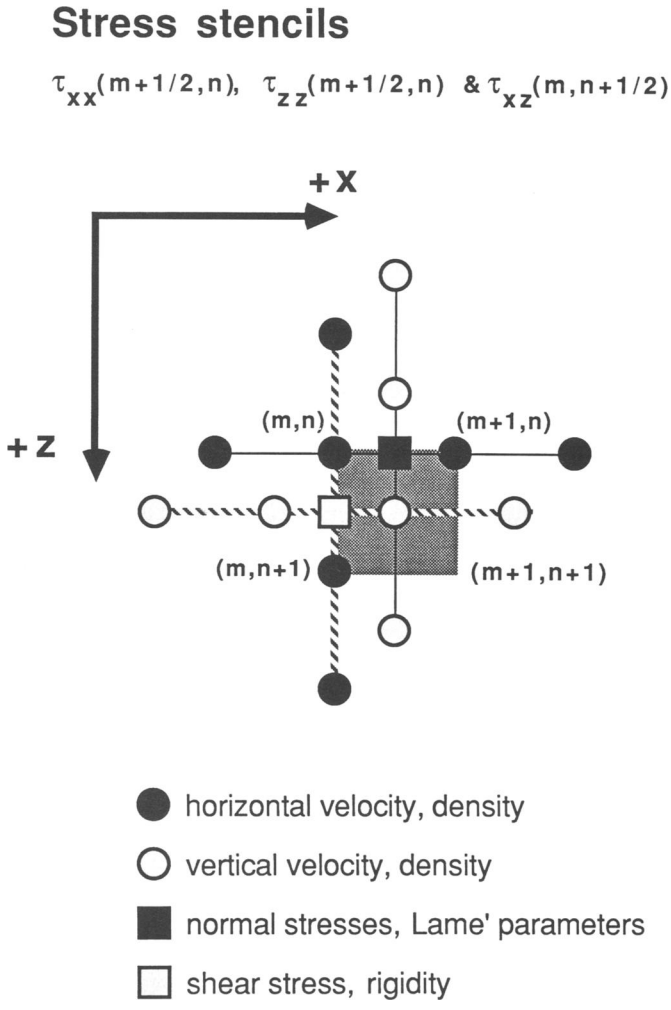

FIG. 2. Staggered finite-difference grid and spatial stencils for the stress update (see Figure 1). The spatial stencil for shear stress is shown as a hachured line with the velocity nodes used in the update. The spatial stencil for the normal stresses is shown as a thin solid line with the velocity nodes used in the update.

where u and w are the displacement components in x and z, u_t and w_t are the particle velocities, τ_{ij} are the stresses, λ and μ are the Lame' parameters with μ the rigidity, and ρ is the density. The compressional velocity is given by $\alpha = \sqrt{[(\lambda + 2\mu)/\rho]}$ and the shear velocity by $\beta = \sqrt{(\mu/\rho)}$.

Equations (1) and (2) are linear first-order coupled equations for particle displacement and velocity, and stress. Taking the first time derivative of equation (2) and substituting particle velocity for displacement provide a first-order system of equations in velocity and stress which can be solved numerically. The difference equations are given in Appendix A. The finite-difference grid is staggered in space as shown in Figures 1 and 2, with velocity components being defined across one diagonal in any given finite-difference cell and stress components being defined across the other. The horizontal velocity component and density are defined at the discrete location (m, n); the vertical component and density are at $(m + 1/2, n + 1/2)$; the normal stresses and Lame' parameters are at $(m + 1/2, n)$; and the tangential stress and rigidity are at $(m, n + 1/2)$. The grid is staggered in both space and time, with the results that for each update the spatial derivatives are centered in space about the variable being updated, and the temporal derivative is centered about the time level of the spatial derivatives. In the scheme I am describing, the time operator is a two point difference of order Δt^2, and the spatial operators are four point differences of order h^4 (see Appendix A). Unlike difference schemes based on the second-order coupled displacement equations, the system has no terms containing spatial derivatives of the material properties. The material properties are always defined at the locations of the quantities they scale. The spatial derivatives can be approximated with an operator of any order accuracy with no difficulty; however, the competing effects of phase advance due to the temporal discretization and phase delay due to the spatial discretization are not well balanced with extremely high-order spatial operators (Dablain, 1986). The numerical boundary conditions become more difficult to solve for long spatial operators as well.

To analyze stability and dispersion properties, we assume a uniform infinite medium which supports a plane wave:

$$\mathbf{u}_t(\mathbf{x}, t) = (u_t, w_t) \exp(\mathbf{k} \cdot \mathbf{x} - \omega t) \tag{4}$$

Taking the difference of the finite-difference solutions for the velocity components at times $\ell + 1$ and ℓ and substituting the constitutive laws into the equation of motion provide a second-order system of $O(\Delta t^2, h^4)$ difference equations in velocities only. We can write this system as a matrix equation using the appropriate finite-difference operators D_{xx}, D_{xz}, D_{zz}, and D_{tt};

$$\underline{0} = \begin{bmatrix} (\alpha^2 D_{xx} + \beta^2 D_{zz}) - D_{tt} & (\alpha^2 - \beta^2) D_{xz} \\ (\alpha^2 - \beta^2) D_{xz} & (\beta^2 D_{xx} + \alpha^2 D_{zz}) - D_{tt} \end{bmatrix} \mathbf{u}_t. \tag{5}$$

The determinant of the matrix is quadratic in D_{tt} and provides the dispersion relations for the numerical scheme. The two roots give the compressional and shear-wave dispersion relations;

$$D_{tt} = \tfrac{1}{2}(\alpha^2 + \beta^2)(D_{xx} + D_{zz}) \pm \tfrac{1}{2}(\alpha^2 - \beta^2)\sqrt{[(D_{xx} + D_{zz})^2 - 4(D_{xx} D_{zz} - D_{xz} D_{xz})]}. \tag{6}$$

Note that the numerical system compressional and shear wave dispersion relations are functions of *both* material velocities when the second term of the radical is nonvanishing, whereas for the continuous system, the second term under the radical is identically zero. The dispersion relations for the $O(\Delta t^2, h^4)$ scheme are given in Appendix B. The stability criterion is given by

$$\Delta t < \frac{h}{\sqrt{2\alpha(c_1 + c_2)}}$$

or

$$\Delta t < 0.606\, h/\alpha, \tag{7}$$

where c_1 and c_2 are the inner and outer coefficients of the fourth-order approximation to the first derivative (see Appendix A). The Δt of relation (7) is smaller than the corresponding stability limit for the second-order staggered-grid scheme by the reciprocal sum of the difference coefficients (see Virieux, 1986). It is also less than the stability limit for the $O(\Delta t^2, h^4)$ approximation to the acoustic wave equation by about 1 percent (see Alford et al., 1974).

The dispersion relations for this scheme are plotted in Figure 3 for different values of Poisson's ratio and for different directions of propagation on the finite-difference grid. Figure 4 shows the sensitivity of the dispersion relation to the choice of time step. From Figures 3 and 4, we see that (1) the shortest shear wavelength on the grid must be sampled at 5 gridpoints/wavelength to minimize the effects of grid dispersion and grid anisotropy, (2) grid dispersion and grid anisotropy are very weakly dependent on Poisson's ratio, (3) grid dispersion is strongest for waves traveling along one of the coordinate directions ($\theta = 0$ degrees), and (4) the scheme can be run at a large fraction of the stability limit to tune the dispersion relation. For example, by running the scheme between 50 percent and 75 percent of the maximum allowed time step (the bottom two curves in Figure 4), we can avoid the unphysically high P-wave phase velocities for sampling less than 13 grid points/wavelength (normalized phase velocity exceeds unity in Figure 4) which result if the scheme is run near the stability limit. Five gridpoint/wavelength sampling is an improvement by a factor of two over that required for $O(\Delta t^2, h^2)$ *P-SV* schemes (Virieux, 1984; Kelly et al., 1976).

For modeling a semiinfinite space, we satisfy the free-surface condition boundary conditions at the $z = 0$ surface

$$\tau_{zz} = 0 = \lambda \frac{\partial u}{\partial x} + (\lambda + \mu) \frac{\partial w}{\partial z}$$

and

$$\tau_{xz} = 0 = \mu\left(\frac{\partial u}{\partial z} + \frac{\partial w}{\partial x}\right). \tag{8}$$

The horizontal derivatives pose no problem. If we assume appropriate symmetry for the stress components about $z = 0$ and extend the grid two nodes above $z = 0$, we can use the boundary conditions to solve for the vertical derivatives and satisfy the free-surface condition. The other boundaries at the grid periphery are coded to satisfy the Clayton-Engquist A1 (1977) absorbing condition.

A spatially localized source is initiated by specifying the appropriate stress components and using the source insertion principle of Alterman and Karal (1968). Either a surface or a

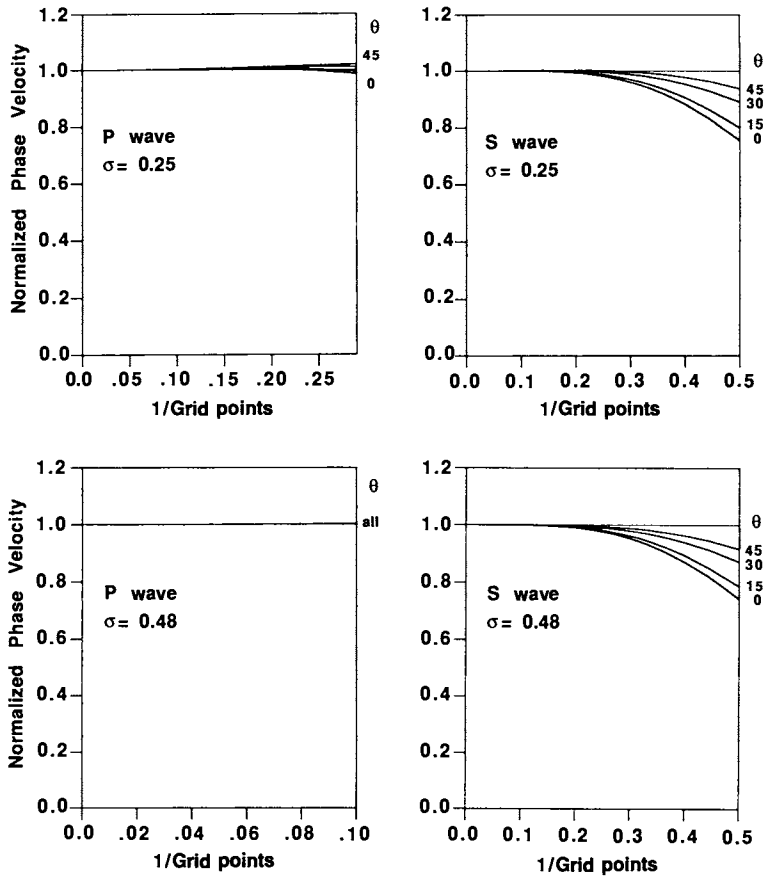

FIG. 3. Numerical dispersion of compressional and shear waves for different values of Poisson's ratio σ, for the finite-difference scheme run at 75 percent of the maximum allowed time step. Each plot has the dispersion curves for propagation at angles of θ = 0, 15, 30, and 45 degrees to the grid, to demonstrate grid anisotropy. The abscissa is plotted in reciprocal sampling (wavelengths/mesh spacing), with the sampling for compressional waves consistent with that for shear waves. On the left are plots of the *P*-wave dispersion for a Poisson's solid (top, $\alpha/\beta = 1.73$), and a high Poisson's ratio material (bottom, $\alpha/\beta \sim 5.0$). Minimum shear-wave sampling to simulate wave propagation in a continuous medium is 5 gridpoints/wavelength.

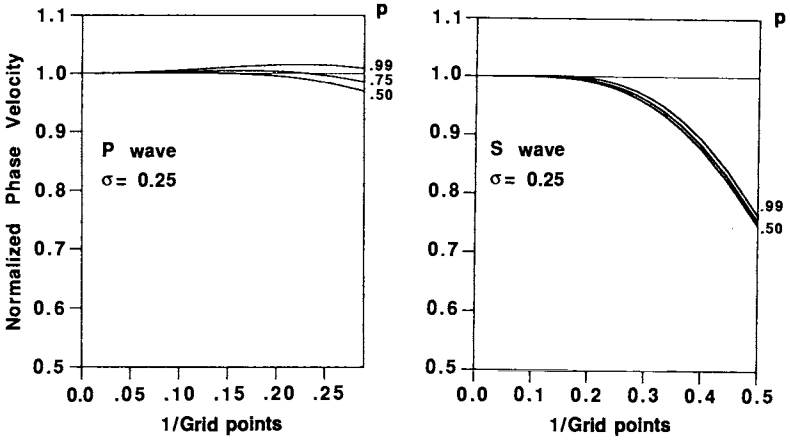

FIG. 4. Dependence of *P* and *S* dispersion on fraction of stability limit. The three dispersion curves shown in each plot are for 99 percent (top), 75 percent, and 50 percent (bottom) of the maximum allowed time step, for waves propagating in one of the coordinate directions in a Poisson solid (see Figure 3). Running the scheme at 50 to 75 percent of the stability limit minimizes the effects of unphysically high phase velocities in *P* and *S* waves near 8.5 and 5 gridpoints/wavelength, respectively.

buried source can be inserted within a small homogeneous region of the grid around the source point.

BENCHMARK TESTS

To examine the fidelity of solutions generated with the $O(\Delta t^2, h^4)$ staggered-grid scheme, I compare finite-difference solutions for Lamb's problem with an exact solution and finite-difference solutions for layered model problems with reflectivity synthetics. The tests are designed to assess the accuracy of (1) waves from a source applied at the free surface, (2) waves propagating in mixed acoustic-elastic media, and (3) waves propagating in low and high Poisson's ratio materials.

Lamb's problem results from the application of a point force in a uniform elastic half-space. In this first finite-difference simulation, I applied a vertical point force to the free surface. The analytical solutions were generated by using Sherwood's (1958) 2-D solution and then convolving the Green's functions with the derivative of the finite-difference source pulse. The geometry is shown in Figure 5. Horizontal and vertical motion seismograms from a Poisson solid are shown in Figures 5 through 7. The finite-difference scheme

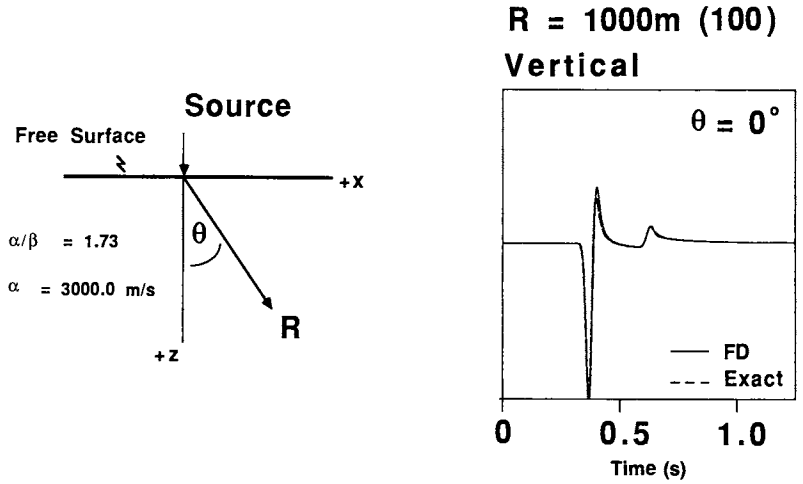

FIG. 5. Lamb's problem geometry (left, model 1 in Table 1) and solution (right). A band-limited vertical point force is applied directly to the free surface of a Poisson solid. The vertical component of motion measured directly below the source (polar angle $\theta = 0$ degrees) is shown. The finite-difference solution is shown as a solid line, the exact solution as a dashed line. The vertical component of motion was observed 1 km (100 grid points) below the free surface. The horizontal component of motion is vanishing at this polar angle. The scheme was run at 75 percent of the stability limit; the 10 percent power level in the source corresponds to 5 gridpoint/wavelength *S*-wave sampling.

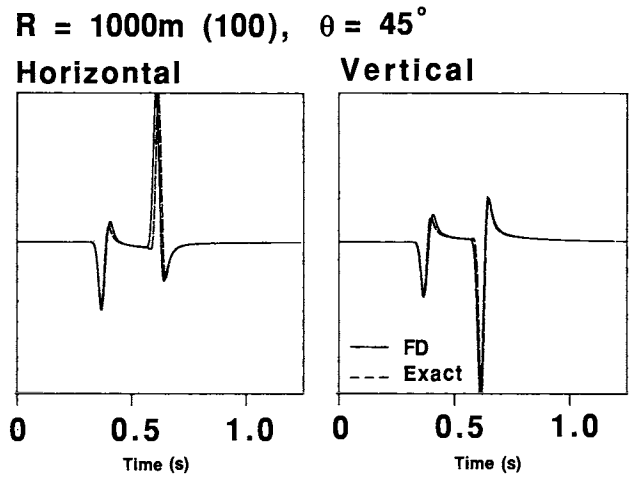

FIG. 6. Lamb's problem solution measured at a polar angle of 45 degrees at a range of 1 km.

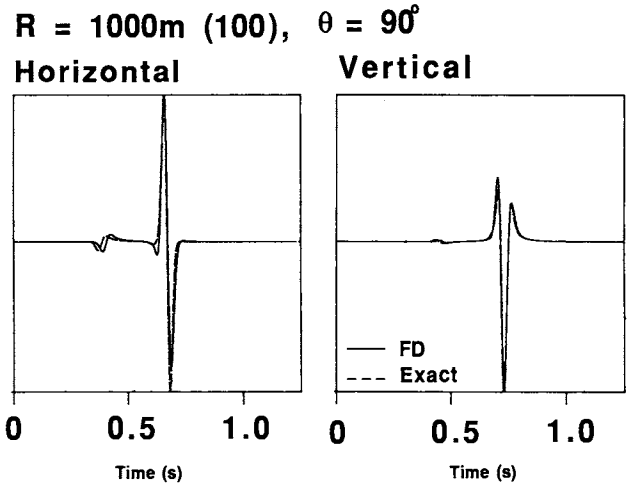

FIG. 7. Lamb's problem solution measured at a polar angle of 90 degrees, along the free surface, at a range of 1 km. On the horizontal component of motion, note the slight timing mismatch in the Rayleigh and *P*-wave arrivals between the two solutions, and the precursor leading the finite-difference Rayleigh wave.

was run at 75 percent of the stability limit and the source pulse was band-limited with the 10 percent power level set for 5 gridpoints per shear wavelength. (For the sake of brevity, I will henceforth refer to 5 gridpoint/wavelength sampling as minimum sampling.) Computational parameters and model material properties for all simulations are given in Table 1.

Minor differences in the timing of the P and S waves or the P and Rayleigh waves can be seen between the finite-difference and analytical solutions. On the synthetics made at the free surface (a polar angle of 90 degrees, Figure 7), a small precursory event leads the Rayleigh wave. I attribute the precursor to grid dispersion. Note that the numerical phase velocities of both P waves sampled with 13 gridpoints/wavelength and shear waves sampled at 8 gridpoints/wavelength exceed unity for waves traveling in a coordinate direction (Figure 4). (The normalized shear-wave velocity only slightly exceeds unity and is not apparent in Figure 4.) For all polar angles, the finite-difference solutions to Lamb's problem are in excellent agreement with the exact solutions, suggesting both that the insertion of the source at the surface is accurate and that the free-surface condition is accurate.

Next I compare finite-difference and reflectivity synthetics from several layered model simulations to examine the accuracy of reflections, wide-angle reflections, head waves, and converted waves. The reflectivity code, Sherwood et al.'s (1983) SOLID program, uses a 2-D line source. After convolving the finite-difference source pulse with the reflectivity Green's functions, the reflectivity and finite-difference synthetics can be compared directly.

The second model is a low-velocity elastic layer over an elastic half-space (model 2 in Table 1). Both materials are Poisson solids, with a velocity contrast between layer and half space of 1 : 2 and no density contrast. This example is designed to test the accuracy of the finite-difference scheme for the simplest possible layered medium. The layer is 195 m thick with a free surface at $z = 0$. A compressive source was initiated in the layer at a depth of 100 m. The 10 percent power level for properly band-limiting shear waves in the low-velocity layer is at 17.3 Hz. Shot records of the vertical component of velocity for offsets from 0 to 2250 m are compared in Figure 8. The agreement between the two sections is very good. Individual traces at several offsets are compared in Figure 9. The finite-difference and reflectivity seismograms are very similar. Minor differences in high-frequency detail are attributable to grid dispersion and to the ripple caused by a wavenumber filter applied to the reflectivity synthetics to reduce wraparound. Note that the finite-difference synthetics faithfully reproduce features at both short and long offsets: i.e., normal incidence reflections and multiples, converted shear waves, head waves and reflected head waves, and Rayleigh waves.

The third model has a water surface layer overlying a Poisson solid half-space. This example is used to demonstrate the ability of the finite-difference scheme to accurately model a mixed acoustic-elastic medium. The layer thickness is again 195 m, with the source at 100 m depth. The water velocity is the lowest nonzero velocity in the model, putting the minimum sampling frequency at 30.0 Hz. The reflectivity and finite-difference vertical velocity shot records are compared in Figure 10. Individual traces at several offsets are displayed in Figure 11. (Although it would be more natural in this example to show pressure seismograms, I have chosen to show the same quantity for all of the simulations.) The agreement between the reflectivity and the finite-difference synthetics is almost exact for every arrival. Note that the records contain a long train of water-bottom multiples, a head wave, and multiply reflected head waves. Very low-amplitude, high-frequency ringing caused by grid dispersion is apparent in the finite-difference synthetics.

Table 1. Model material properties and computational parameters.

Model	Layer	Thickness (m)	α (m/s)	β (m/s)	σ	ρ (g/cm³)	h (m)	Δt (ms)	f_{max} (Hz)
(1) Lamb	1	half-space	3000	1730	0.25	2.5	10	1.531	35
(2) Elastic/elastic	1	195	1500	865	0.25	2.5	10	1.531	17.3
	2	half-space	3000	1730	0.25	2.5			
(3) Acoustic/elastic	1	195	1500	0	0.50	1.0	10	1.531	30.0
	2	half-space	3000	1730	0.25	2.5			
(4) Transition	1	195	1500	0	0.50	1.0	10	1.531	15.0*
	2	200	2250	750	0.438	1.75			30.0†
	3	half-space	3000	1730	0.25	2.5			
(5) (Low/high Poisson's ratios)	1	198	4000	800	0.479	2.5	7.62	0.866	21.0
	2	half-space	6000	3460	0.25	2.5			
(6) (Free surface stability)	1	125‡	1300	600	0.365	1.0	25	3.281	4.8
	2	half-space	3500	2000	0.258	2.6			
(7) (Perturbed acoustic/elastic)	1	100§	1500	0	0.50	1.0	10	1.531	30.0
	2	half-space	3000	1730	0.25	2.5			

*First simulation
†Second simulation same model
‡Extended 2000 m horizontally
§Mean layer thickness

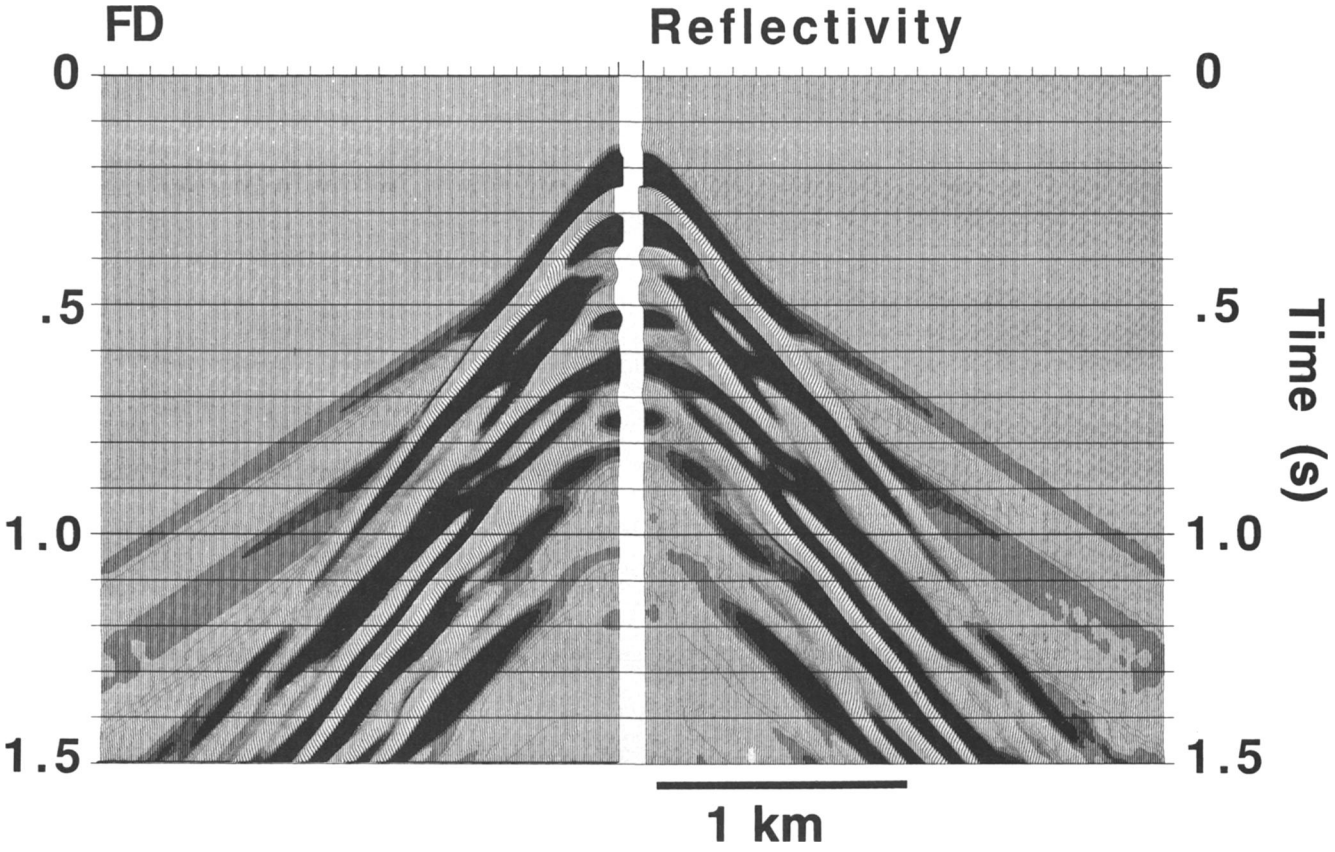

FIG. 8. Free-surface vertical component of motion comparing finite-difference (left) and SOLID reflectivity (right) shot records for a simple low-velocity elastic layer and high-velocity half-space model (model 2, Table 1). Both the layer and the half-space are Poisson solids. The source was buried at a depth of 100 m in a 195 m thick layer. Note that the direct wave is clipped. The polarity of the plots was reversed to enhance the first arrivals. The slight ripple in the reflectivity solutions (seen most easily on the head waves) is the result of a low-pass wavenumber filter used to suppress wraparound.

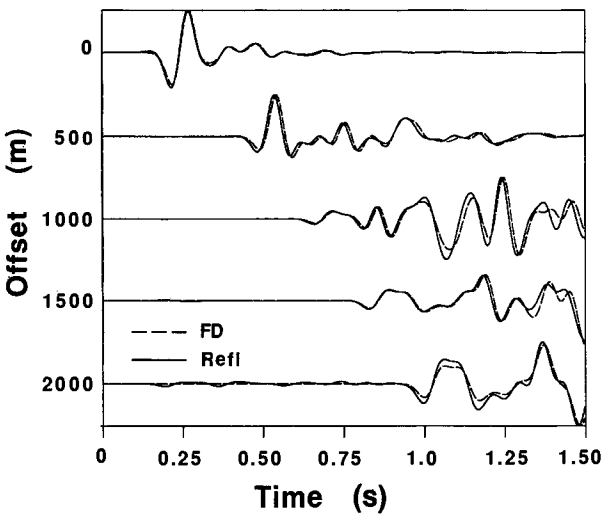

FIG. 9. Comparison of individual traces from the shot records in Figure 8, shown for different offsets. Each pair of traces is normalized independently. In these and subsequent plots the finite-difference seismograms are shown as the dashed lines. The magnitude of the ripple caused by the wavenumber filter on the reflectivity synthetics can be seen as the motion leading the head wave on the trace at 2000 m offset.

The fourth model includes a low Poisson's ratio material sandwiched between a water surface layer and an elastic half-space (see Table 1). This model is designed to test the stability of the finite-difference scheme for low shear velocities similar to the water bottom in a marine survey. The transition layer compressional velocity is the average of that of the water layer and the half-space; the shear velocity was one-third of the compressional velocity. (Poisson's ratio in the transition layer is 0.438.) The transition layer was 200 m thick and the source was in the water layer at a depth of 100 m. A maximum frequency in the source pulse of 15 Hz corresponds to the minimum sampling of shear waves in the transition layer. Agreement between the vertical-component reflectivity and finite-difference traces is very good (Figure 12). In this model the maximum frequency for proper shear-wave sampling is controlled by the low shear velocity in the transition layer, which is often the case in modeling marine problems. To test the stability of the scheme for undersampled shear waves, the model was rerun with a 30 Hz source. In this second simulation, high-frequency converted shear waves in the transition zone were sampled at 2.5 gridpoints/wavelength. Figure 13 compares the finite-difference traces with the reflectivity synthetics. The traces are different for PSP arrivals which propagated in the transition region (offset of 1000 m at 1.25 s). This

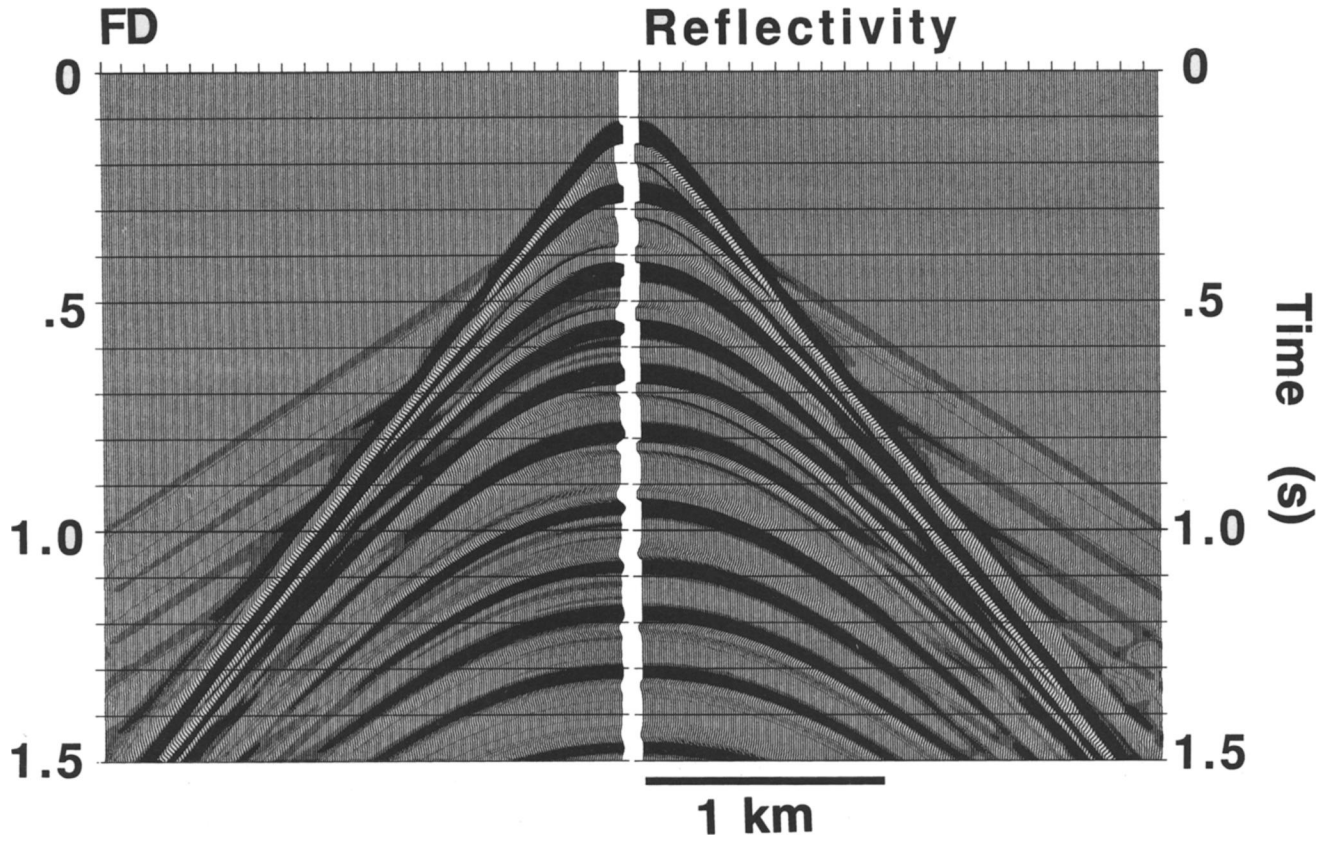

FIG. 10. Free-surface vertical component of motion comparing finite-difference and SOLID reflectivity shot records for an acoustic layer and elastic half-space model (model 3, Table 1). Note that the direct wave, the reflection, and several multiples are clipped. The polarity of the plots was reversed to enhance the first arrivals. The edge effect at long offsets in the reflectivity synthetics is wraparound.

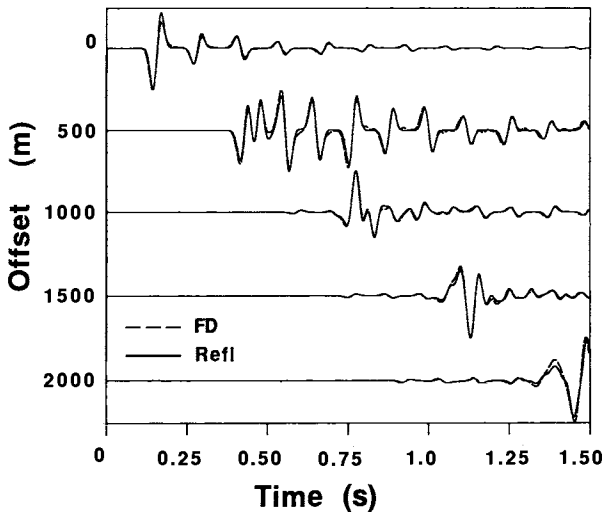

FIG. 11. Comparison of individual traces from the shot records in Figure 10. Each pair of traces is normalized independently.

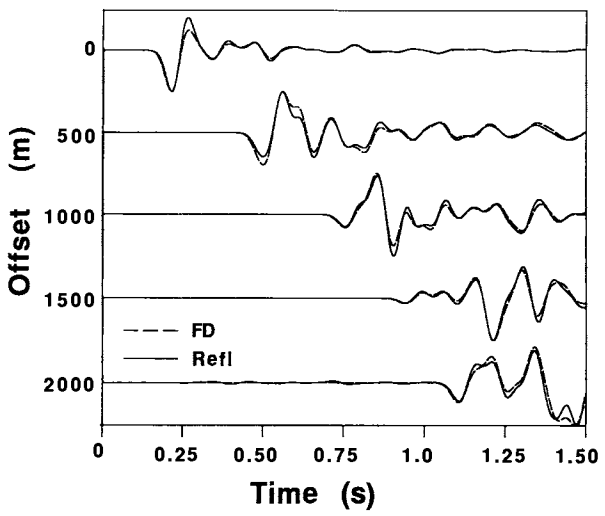

FIG. 12. Comparison of vertical component traces from shot records of high Poisson's ratio transition region model (model 4). The surface layer is water, the transition layer has an α/β ratio of 3; and the half-space is a Poisson solid. The source has been band-limited so that converted shear waves in the transition region are sampled at 5 gridpoints/wavelength. Each trace is normalized independently.

simulation indicates (1) that the finite-difference scheme is stable even if the shear waves in a low shear velocity, high Poisson's ratio material are severely undersampled, and (2) that compressional waves are accurately modeled even if the shear waves are not.

The last layered model (model 5) tested the accuracy of the free-surface condition for a high Poisson's ratio surface layer. The layer is 200 m thick, with a source at 100 m depth. Poisson's ratio in the surface layer is 0.479, corresponding to a compressional-to-shear velocity ratio of 5 : 1. Individual traces of horizontal and vertical velocity are compared to the reflectivity synthetics in Figure 14. The horizontal-motion synthetics are in good agreement at all offsets. The vertical-motion finite-difference synthetics agree in low-frequency character with the reflectivity synthetics but differ in high-frequency character at the arrivals of a critically refracted *PSP* free-surface wave. This arrival can be seen on the vertical component lagging the direct wave by about 0.25 s, and traveling with a speed near that of the compressional velocity of the surface layer (4000 m/s). The *PSP* wave is entirely a free-surface effect, which results in evanescent decay of the converted *P* wave away from the boundary and angle-dependent phase shifts in both *P* and *S* reflected waves. The discrepancy between the finite-difference and reflectivity solutions is attributable to two causes: (1) the manner in which the $z = 0$ boundary condition is satisfied and (2) shear-wave phase velocity error due to coarse sampling. In the reflectivity code, the vacuum is modeled as a half-space with very low compressional and shear velocities and density, whereas the finite-difference code satisfies the vanishing stress conditions explicitly. The higher frequencies in the finite-difference simulation are minimally sampled (at 5 gridpoints/wavelength) when propagating as converted shear waves in the layer. The phase error along the shear wave path may be an eighth to a quarter cycle for the longer wavelength.

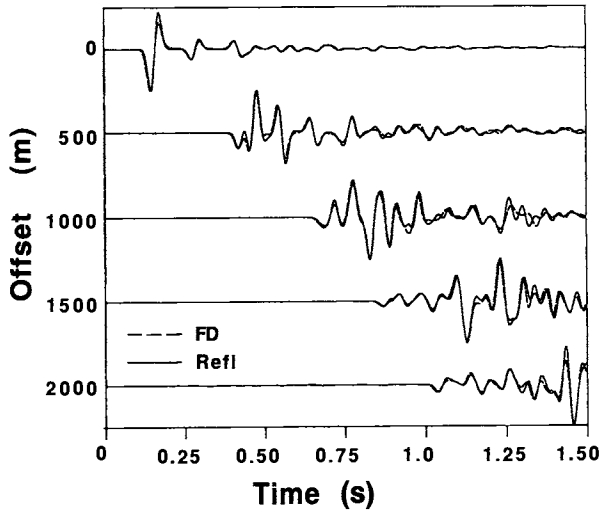

FIG. 13. Comparison of vertical component traces from shot records of a high Poisson's ratio transition region model in which high frequency in the source was doubled relative to the previous figure (model 4, second simulation). These synthetics demonstrate that the finite-difference scheme is stable and accurately models *P*-wave propagation even if the shear waves are grossly undersampled. In the transition region the converted shear waves are sampled at 2.5 gridpoints/wavelength. Mismatched arrivals at $x = 1000$ m at $t = 1.25$ s correspond to *PSP* reflections. Each trace is normalized independently.

LATERALLY HETEROGENEOUS MODELS

To test the stability of the numerical free-surface boundary condition in the presence of lateral inhomogeneity, I replicated a model experiment by Vidale and Clayton (1986). They compared the stability of different numerical formulations of the free-surface boundary conditions for *P-SV* displacement equation schemes. The geometry and computational parameters which I used (model 6 in Table 1) were as close as possible to those used by Vidale and Clayton (1986). Seismograms from

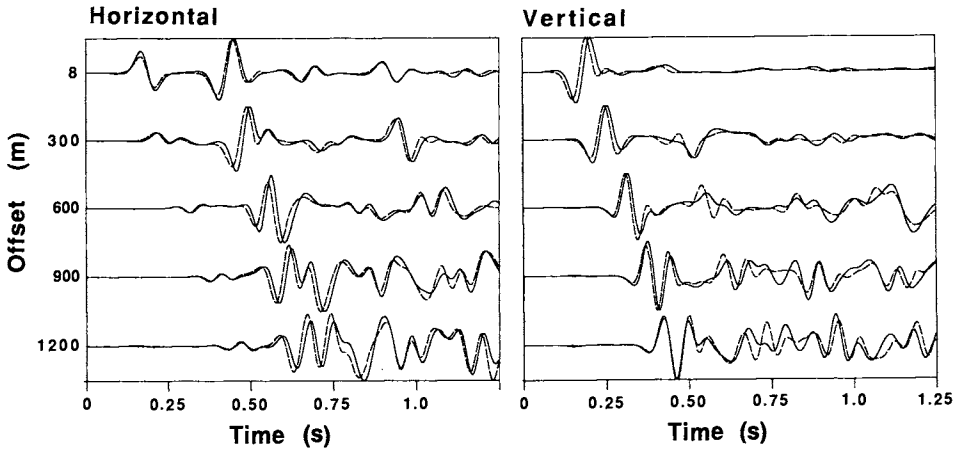

FIG. 14. Horizontal and vertical component traces from high Poisson's ratio surface layer model (model 5). The surface layer $\alpha/\beta = 5.0$. The low frequency character of the reflectivity synthetics is well matched by the finite-difference synthetics. The detail in the vertical component of motion is different at the time of the *PSP* arrival (see text). Each trace is normalized independently.

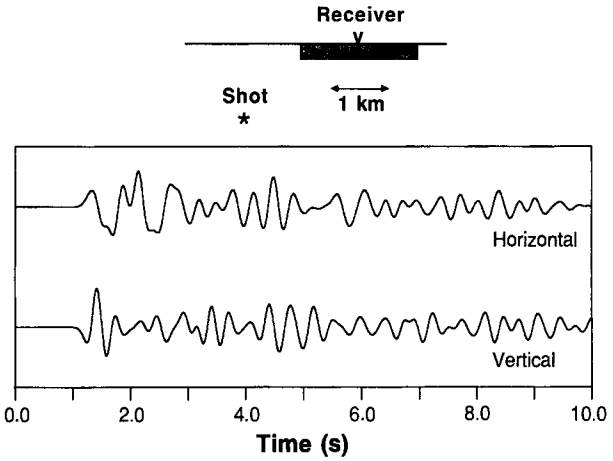

FIG. 15. Test of the free-surface condition in the presence of a laterally heterogeneous surface structure (model 6). The filled notch at the free-surface has a compressional velocity of 1.3 km/s, a shear velocity of 0.6 km/s, a density of 1.0 g/cm^3, and a thickness of 0.10 km. The half-space has velocities of 3.5 and 2.0 km/s and a density of 2.6 g/cm^3. Compare to Figure 3 in Vidale and Clayton (1986). The dominant frequency in this simulation is about 20 percent lower than that of Vidale and Clayton's simulation. True amplitude traces are shown.

the test are shown in Figure 15. They are similar to those calculated by Vidale and Clayton using both their implicit approximation to the free-surface boundary condition and the often-used one-sided approximation to the free-surface condition (Ilan et al., 1975). The test indicates that the free-surface formulation is robust for models having laterally heterogeneity at and near the free-surface.

A seventh model consists of a water layer with an irregular boundary. The model and synthetic shot record are shown in Figure 16. To the left of the shotpoint, the model is identical to that used in the plane-layered acoustic-elastic test (Figure 10), while to the right of the shotpoint, the water-elastic interface has a cosine irregularity which is 100 m in amplitude and extends 1 km. The shot record shows the deformation of the head wave and a complicated series of reflections and diffractions caused by the irregularity. In this simulation, the irregular surface is not aligned uniformly along one of the coordinate directions; the results demonstrate that the scheme is stable for modeling arbitrarily oriented interfaces separating acoustic and elastic media. The staggered-grid scheme allows for arbitrarily oriented interfaces at abrupt acoustic-elastic interfaces without the need for specialized code for boundary conditions (Stephen, 1983, 1984).

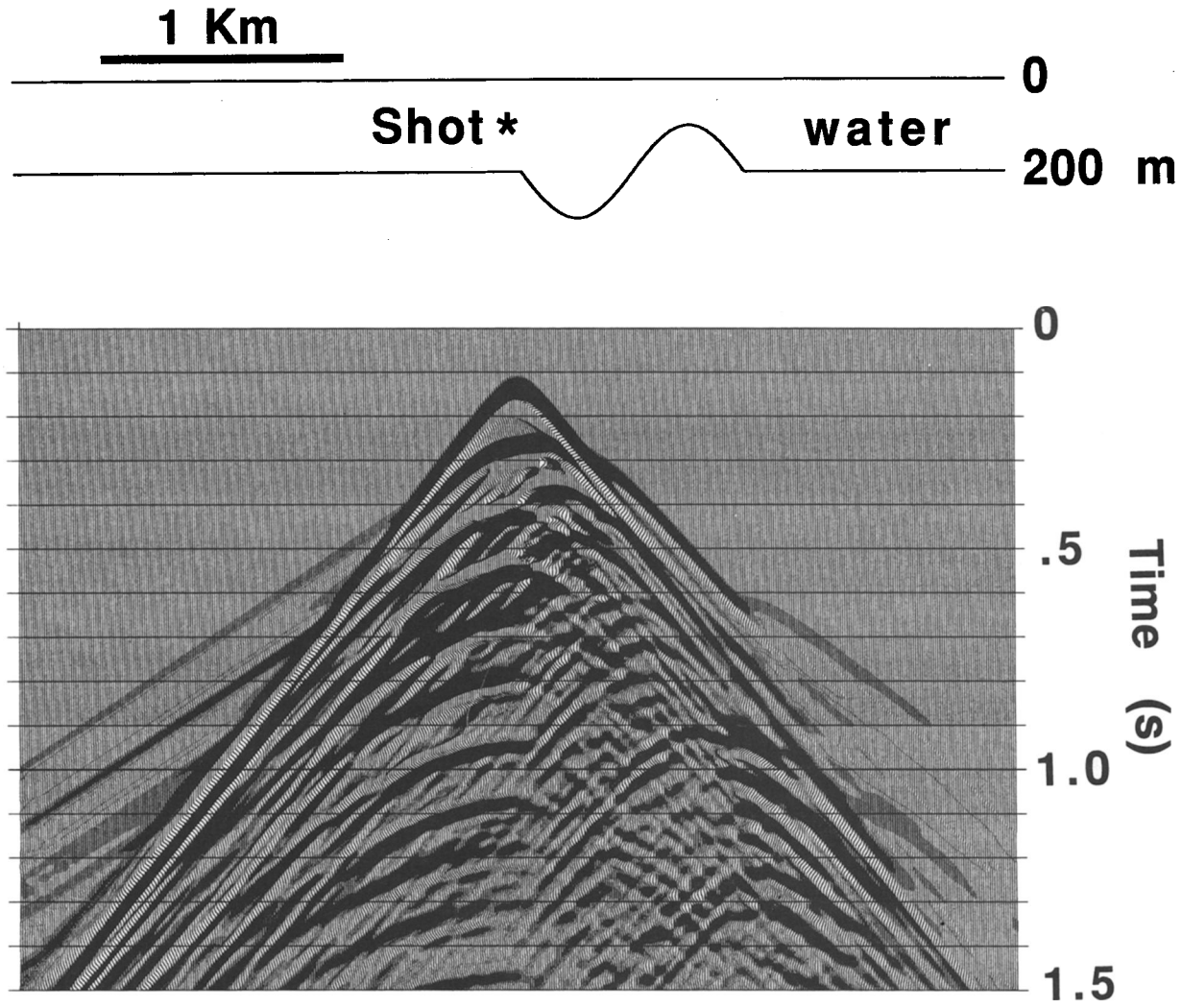

FIG. 16. Vertical component shot record measured at $z = 0$ for model 7, in which the water layer has an irregular bottom. Note the disruption of the head wave and the reflection and multiples from the steep slope of the perturbed interface. The model to the left of the shotpoint is identical to the plane-layered acoustic-elastic model, simulations from which are shown in Figure 10.

DISCUSSION AND CONCLUSIONS

The Madariaga-Virieux staggered-grid scheme is easily written with higher order approximations to the spatial derivatives, making it more efficient than other schemes for most modeling problems. Comparisons of finite-difference and reflectivity synthetics from models with acoustic and elastic layers, and from models with low Poisson ratio layers, show that the finite-difference scheme is stable and accurate for a wide range of compressional to shear velocity ratios. The results from models with near-surface lateral heterogeneity and with laterally heterogeneous acoustic layers suggest that the scheme is suitable for modeling a broad class of problems found in exploration seismology.

To calculate the same bandwidth, the 2-D fourth-order accurate scheme requires one-quarter as many nodes as second-order *P-SV* methods. In a fixed memory machine this scheme can generate twice the bandwidth with the same number of nodes as a second-order scheme. It is difficult to compare rigorously different types of finite-difference schemes because storage and calculations per node can vary significantly depending on the formulation. This 2-D fourth-order staggered-grid, velocity-stress *P-SV* scheme requires 14 percent more storage and approximately the same computation time as 2-D fourth-order schemes written in displacements. The advantages of the staggered-grid scheme lie in its stability and accuracy for modeling large Poisson's ratio materials and mixed acoustic-elastic media, and in the ease with which sources can be inserted at and near the free-surface. This code should be particularly useful for modeling near-surface problems, and for amplitude-offset studies in laterally varying media.

ACKNOWLEDGMENTS

I would like to thank the Chevron Oil Field Research Laboratory for supporting development of the finite-difference scheme. Some of the benchmark tests were supported by the National Science Foundation under grant EAR-8608776. I would also like to thank Fred Hilterman and John Sherwood for the reflectivity synthetics, and Dave Hale and Bill Symes for many discussions about finite-difference methods.

REFERENCES

Alterman, Z., and Karal, F. C., 1968, Propagation of elastic waves in layered media by finite difference methods: Bull. Seis. Soc. Am., **58**, 367–398.

Alford, R. M., Kelly, K. R., and Boore, D. M., 1974, Accuracy of finite-difference modeling of the acoustic wave equation: Geophysics, **39**, 834–852.

Bayliss, A., Jordan, K. E., LeMesurier, B. J., and Turkel, E., 1986, A fourth-order accurate finite-difference scheme for the computation of elastic waves: Bull. Seis. Soc. Am., **76**, 1115–1132.

Clayton, R., and Engquist, B., 1977, Absorbing boundary conditions for acoustic and elastic wave equations: Bull. Seis. Soc. Am., **67**, 1529–1540.

Dablain, M. A., 1986, The application of higher-order differencing to the scalar wave equation: Geophysics, **51**, 54–66.

Ilan, A., Ungar, A. U., and Alterman, Z., 1975, An improved representation of boundary conditions in finite-difference schemes for seismological problems: Geophys. J. Roy. Astr. Soc., **43**, 727–745.

Kelly, K. R., Ward, R. W. Treitel, S., and Alford, R. M., 1976, Synthetic seismograms: A finite-difference approach: Geophysics, **41**, 2–27.

Madariaga, R., 1976, Dynamics of an expanding circular fault: Bull. Seis. Soc. Am., **66**, 639–666.

Sherwood, J. W. C., 1958, Elastic wave propagation in a semi-infinite solid medium: Proc. of the Physical Soc., **71**, 207–219.

Sherwood, J. W. C., Hilterman, F. J., Neale, R. N., and Chen, K. C., 1983, Synthetic seismograms with offset for a layered elastic medium: Offshore Tech. Conf. Abstracts, 539–543.

Stephen, R. A., 1983, A comparison of finite difference and reflectivity seismograms for marine models: Geophys. J. Roy. Astr. Soc., **72**, 39–57.

——— 1984, Finite difference seismograms for laterally varying marine models: Geophys. J. Roy. Astr. Soc., **79**, 185–198.

Vidale, J. E., and Clayton, R. W., 1986, A stable free-surface boundary condition for two-dimensional elastic finite-difference wave simulation: Geophysics, **51**, 2247–2249.

Virieux, J., 1984, *SH*-wave propagation in heterogeneous media: Velocity-stress finite-difference method: Geophysics, **49**, 1933–1957.

——— 1986, *P-SV* wave propagation in heterogeneous media: velocity-stress finite-difference method: Geophysics, **51**, 889–901.

APPENDIX A

FINITE-DIFFERENCE EQUATIONS

First discretize the x, z, and t coordinates and the field variables , letting $x = mh$ or $x = (m \pm 1/2)h$, $z = nh$ or $z = (n \pm 1/2)h$, and $t = \ell\Delta t$ or $t = (\ell \pm 1/2)\Delta t$; h is the finite-difference grid spacing and Δt is the finite-difference time sample. The field variables are defined at the locations shown in Figures 1 and 2. The difference equations are given by

$$
\begin{aligned}
D_t^+ u_t(m, n, \ell - 1/2) &= 1/\rho(m, n)[D_x^- \tau_{xx}(m + 1/2, n, \ell) + D_z^- \tau_{xz}(m, n + 1/2, \ell)], \\
D_t^+ w_t(m + 1/2, n + 1/2, \ell - 1/2) &= 1/\rho(m + 1/2, n + 1/2)[D_x^+ \tau_{xz}(m, n + 1/2, \ell) + D_z^+ \tau_{zz}(m + 1/2, n, \ell)], \\
D_t^+ \tau_{xx}(m + 1/2, n, \ell) &= [\lambda(m + 1/2, n) + 2\mu(m + 1/2, n)]D_x^+ u_t(m, n, \ell + 1/2) \\
&\quad + \lambda(m + 1/2, n)D_z^- w_t(m + 1/2, n + 1/2, \ell + 1/2), \\
D_t^+ \tau_{xz}(m, n + 1/2, \ell) &= \mu(m, n + 1/2)[D_z^+ u_t(m, n, \ell + 1/2) + D_x^- w_t(m + 1/2, n + 1/2, \ell + 1/2)],
\end{aligned}
\tag{A-1}
$$

and

$$
\begin{aligned}
D_t^+ \tau_{zz}(m + 1/2, n, \ell) &= [\lambda(m + 1/2, n) + 2\mu(m + 1/2, n)]D_z^- w_t(m + 1/2, n + 1/2, \ell + 1/2) \\
&\quad + \lambda(m + 1/2, n)D_x^+ u_t(m, n, \ell + 1/2),
\end{aligned}
$$

where D_t^+ is the forward difference operator in time, and $D_x^{\pm}$ and $D_z^{\pm}$ are the forward or reverse difference operators in space, with the sign chosen to center the difference operator about the quantity being updated. For example, the spatial derivative of the normal stress component used in the update for particle velocity is given by

$$D_x^- \tau_{xx}(m+1/2, n, \ell) = -c_2\left[\tau_{xx}(m+3/2, n, \ell) - \tau_{xx}(m-3/2, n, \ell)\right] + c_1\left[\tau_{xx}(m+1/2, n, \ell) - \tau_{xx}(m-1/2, n, \ell)\right], \quad \text{(A-2)}$$

where c_1 and c_2 are the inner and outer difference coefficients for the fourth-order approximation to the first derivative, 9/8 and 1/24, respectively.

APPENDIX B

FINITE-DIFFERENCE DISPERSION RELATION

The dispersion relation for the $O(\Delta t^2, h^4)$ scheme is developed by substituting the difference coefficients into equation (6) and evaluating the expression

$$\begin{aligned}
\sin^2(\omega\Delta t/2) = \frac{(\Delta t\alpha)^2}{h^2}\Big\{ & \tfrac{1}{2}(1+\beta^2/\alpha^2)\Big\{\Big[c_1^2 + 2c_1c_2\left[1 - 4\cos^2(k_x h/2)\right]\Big]\sin^2(k_x h/2) + c_2^2(3k_x h/2) \\
& + \left[c_1^2 + 2c_1c_2\Big[1 - 4\cos^2(k_z h/2)\Big]\right]\sin^2(k_z h/2) + c_2^2\sin^2(3k_z h/2)\Big\} \\
& \pm \tfrac{1}{2}(1-\beta^2/\alpha^2)\Big[\Big(\Big[c_1^2 + 2c_1c_2\Big[1 - 4\cos^2(k_x h/2)\Big]\Big]\sin^2(k_x h/2) + c_2^2\sin^2(3k_x h/2) \\
& + \left[c_1^2 + 2c_1c_2\Big[1 - 4\cos^2(k_z h/2)\Big]\right]\sin^2(k_z h/2) + c_2^2\sin^2(3k_z h/2)\Big)^2 \\
& - 4\Big\{\Big(\Big[c_1^2 + 2c_1c_2\Big[1 - 4\cos^2(k_x h/2)\Big]\Big]\sin^2(k_x h/2) + c_2^2\sin^2(3k_x h/2)\Big) \\
& \times \Big(\Big[c_1^2 + 2c_1c_2\Big[1 - 4\cos^2(k_z h/2)\Big]\Big]\sin^2(k_z h/2) + c_2^2\sin^2(3k_z h/2)\Big) \\
& - \Big[c_1^2(\cos((k_x + k_z)h/2) - \cos((k_x - k_z)h/2) + c_2^2(\cos(3(k_x + k_z)h/2) - \cos(3(k_x - k_z)h/2)) \\
& + c_1c_2(\cos((3k_x - k_z)h/2) - \cos((3k_x + k_z)h/2) + \cos((3k_z - k_x)h/2) - \cos((3k_z + k_x)h/2))\Big]^2/4\Big\}\Big]^{1/2}\Big\}.
\end{aligned} \quad \text{(B-1)}$$

The positive sign on the radical gives the dispersion relation for compressional waves, and the negative sign gives the dispersion relation for shear waves. The stability criterion is established by demanding that ω be real and by examining the magnitude of the right-hand side. The stability criterion is about 1 percent lower than that for the fourth-order acoustic wave, finite-difference scheme described in Alford et al. (1974). See equation (7) in the text.